Engineering Structures 273 (2022) 115057

Contents lists available at ScienceDirect

Engineering Structures

journal homepage: www.elsevier.com/locate/engstruct

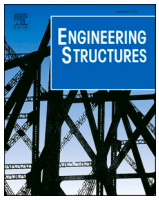

Numerical simulations of the sliding impact between an ice floe and a ship hull structure in ABAQUS

Jianan Zhang [a], Zhenhui Liu [b,*], Muk Chen Ong [a], Wenyong Tang [c]

[a] Department of Mechanical and Structural Engineering and Materials Science, University of Stavanger, Kjell Arholms gate 41, 4021 Stavanger, Norway
[b] Department of Mechanical and Marine Engineering, Western Norway University of Applied Sciences, 5528 Haugesund, Norway
[c] School of Naval Architecture, Ocean & Civil Engineering, Shanghai Jiao Tong University, Shanghai 200240, China

ARTICLE INFO

Keywords:
Sliding impact
Ice material
VUMAT
Steel fracture
Internal energy
Plastic dissipated energy
Static friction
Dynamic friction

ABSTRACT

This paper studies the hull structural responses of a steel grillage subjected to sliding ice loads, which have been rarely investigated in the literature. Sliding ice loads are modelled using nonlinear finite element analysis (NLFEA) method; and Abaqus Explicit is adopted as the numerical solver. Deformations and damages of ice and steel are both considered. A rigid ice model is also simulated for comparison purposes. The hull's local structural responses under different load cases, including deformation, contact forces, and energy distribution, have been analysed. The effects of static structure-to-structure friction coefficient and the relative stiffness between ice and structure are studied. It is found that the deformation of structures will increase the total friction coefficient, which is defined as the ratio of the friction force (the tangential contact force) to the normal contact force. When the ice floe is considered rigid, the static friction coefficient has little effect on the local structural responses of the hull. If using a higher-strength steel material for hull structures in the ice-classed ship design, the hull's deflection and total friction decrease, and the hull dissipates less energy as expected. Moreover, stationary load cases with the same loading condition in the normal direction as sliding load cases are also simulated. When using the deformable ice material model, the simulation results show that the hull's final contact forces and deflection in stationary load cases are larger than those in sliding load cases. Besides, the effect of steel material is more significant in stationary load cases than in sliding load cases.

1. Introduction

During a ship sailing in the water with ice floes, the hull structures may be impacted by ice floes at the vicinity of the waterline. The ice impacts tend to move along the hull due to relative motions between the ship and the ice floes. One example is the "Reduta Ordona" bulk carrier, damaged by a growler iceberg with a sliding impact in 1996, shown in Fig. 1 [1]. Another example is the famous Titanic disaster that happened in 1912, which was probably caused by the long sliding impact between the ship hull and the iceberg, and several compartments got flooded [2,3]. The effect of sliding ice load makes a difference to the structure's load-bearing capacity based on experimental and numerical studies [4–6]. The hull structure's load-bearing capacity is much weaker under the impact of moving ice loads than stationary loads when plastic responses of the hull are induced [6]. However, the tangential motion of ice loads has little influence on the hull's load-bearing capacity when the hull remains elastic [6]. Liu and Amdahl [7–8] developed the 'slide' mechanism in the analytical theories about the ice-ship impacts. Song et al. [9] presented case studies on calculating the sliding loads of iceberg impact adopting such analytical equations. The energy-based calculation method for ice loads has ignored the energy due to the sliding mechanism, as shown in Dolny [10] and Daley [11]. The impulse-based analytical theory deals with the global rigid body dynamics assuming a short impact duration. It is not applicable to capture the local deformation during the long duration sliding impact, even though the same word 'slide' is used. The nonlinear finite element analysis (NLFEA) methods shall be used to capture the local deformations.

The research on structural responses of offshore structures under ice moving loads (the sliding effect) is quite limited; however, there is a lot of work on moving loads in ship grounding scenarios. Some main features of this complex grounding process are large contact forces, the extensive damage of hull structure, and the high nonlinearity [12,13]. These characteristics can be observed in both grounding and iceberg

* Corresponding author.
E-mail addresses: zhli@hvl.no, zhenhui.liu@outlook.com (Z. Liu).

https://doi.org/10.1016/j.engstruct.2022.115057
Received 9 March 2022; Received in revised form 17 September 2022; Accepted 28 September 2022
Available online 13 October 2022

Fig. 1. The bulk carrier "Reduta Ordona" collided with a growler in Hudson Strait on its way from Poland to Churchill, Manitoba, July 21, 1996 [1].

sliding scenarios. In previous numerical studies of ship grounding, the seabed indenters are often considered rigid, shown in Alsos and Amdahl [14].

In numerical studies of ice moving loads on ship structures, ice indenters are also usually assumed to be rigid. Quinton et al. [6] used a rigid ice indenter to study static and moving ice loads in the MPP-DYNA, a sub-version of LS-DYNA. Quinton [15] later applied a moving ice load patch to plated structures with a rigid plate indenter which had the same dimensions as the ice load patch defined by the IACS polar class [16]. The rigid ice indenter overestimates the stiffness of ice. Kim and Quinton [4] chose a crushable foam material model in LS-DYNA based on a user-defined stress-volumetric strain relationship, initially proposed by Gagnon and Derradji-Aouat [17]. However, the crushable foam model cannot simulate the local ice failure behaviours, which is crucial in studying sliding ice impacts. Additionally, inputs to the model do not have physical meanings. Therefore, this ice material model has limitations on simulating structural responses under moving ice loads. Ince et al. (2017a) [18] proposed a new constitutive equation on ice materials and applied it on simulating ice-structure interactions (see Ince et al., 2017b [19]). The ice failure is simulated by using the cohesive zone method (CZM). The confining effects (pressure dependency of ice strength) are not included in their studies. Another challenge for the study on sliding ice loads is that the ship's and the ice floe's motions may change due to the impact force and the surrounding water, as the impact duration is usually long during the sliding impacts. This phenomenon is relevant to the so-called "external mechanics" for the ship collision study [20]. Gagnon and Wang [21] performed global simulations of iceberg impacts including the hydrodynamics by utilizing the ALE formulation in LS-DYNA. Yu and Amdahl [22] simulated the hydrostatic loads using user-defined loads in LS-DYNA to study the ship and iceberg impacts. These methods are either time-consuming or have numerical instability problems, consequently not suitable for performing detailed studies of the local interactions.

Sea ice mechanical properties depend on ice formation and its growth processes. The first-year ice has obvious anisotropic properties, while multi-year ice can be considered isotropic because of the chaotic arrangement of crystals in multi-year ice [23]. We assume that the ice floes are isotropic in this study, as mentioned by Sanderson [24]. Moreover, the strain rate of ice also influences ice mechanics. At high strain rate ($>10^{-3}$ s^{-1}) scenarios, such as ice collision, the dominant failure mode of ice is brittle failure [24]. There are a few types of commonly used phenomenological ice models, such as crushable foam [25,26], elastic–plastic model [27–31], and viscous model [32–36]. Among these models, different yield or failure criteria based on experimental data are adopted to describe the ice failure process. For cases based on the classic plasticity theory, the yield and failure criteria are two different criteria. As for the cases that do not consider plasticity, the yield criterion acts as a failure criterion. Commonly used yield criteria include von Mises [37,38], Tsai-Wu [39 27,32,40–42], Mohr-Coulomb [35,43–45], and Drucker-Prager [46–48]. The Tsai-Wu yield criterion has been widely applied to freshwater ice and icebergs. It is usually written as a function of hydrostatic pressure and von-Mises stress. This criterion can also be expressed as a function of hydrostatic pressure and the second invariant of deviatoric stress tensor [27]. The constants in the Tsai-Wu yield function were determined by experimental data reported by literature [40–42]. Liu et al. [27] adopted the Tsai-Wu yield criterion in the developed elastic-perfectly ice material. They proposed a user-defined empirical failure criterion based on the effective plastic strain and the hydrostatic pressure. Xu et al. [32] also incorporated the Tsai-Wu yield criterion in the proposed viscoelastic-plastic material model. In this paper, the elastic-perfectly ice material model is employed as it is suitable for simulating the ice-structure interactions.

Unlike the ice failure, the failure of steel material has been well developed both theoretically and numerically. The material failure model usually needs to be calibrated with experimental test data under various stress states, see the work by Bai and Wibercik [49] and Kõrgesaar and Romanoff [50]. In fact, the experimental test data are not always available for a specific material grade, and the material test data also have statistical characteristics. Ice-classed ships are always designed with marginal deformations towards the exposure of ice loads. Consequently, moderate plasticity is expected to be observed, which indicates that the failure of the steel may have second-order effects in the ice and structure interactions (ice-classed ships), especially if a deformable ice material is going to be used in the simulation.

This paper investigates ice moving loads on a steel grillage by simulating an ice floe sliding along the hull using ABAQUS software [51]. The novelty of the present study is that detailed numerical studies have been done for the local ice-hull interactions, including the failures of both ice and steel (i.e., a shared-energy design method). Detailed parametric studies about the deformation, contact forces, and energy distribution have been performed. The grillage is designed according to FSICR IA Super class [52]. It is subjected to a displacement-controlled ice floe with combined vertical indenting and horizontal sliding. A user-defined elastic-perfectly plastic ice material model is employed to simulate the ice failure behaviours in this work. For comparison, the iceberg is also modelled as a rigid body. Different friction coefficients are investigated, and two steel materials (i.e., S235 and S350) are also employed in the numerical simulations for simulating relatively strong (ice-classed ship) and weak (non-ice-classed ship) structure stiffness.

2. Methodology

From the structure design point of view, the structure design principle could be categorized as follows [25]:

- Ductile design. The ship structure is more vulnerable to deformations during an impact.
- Shared-energy design. The ship and the impact object share the impact energy. The ship and the iceberg have similar stiffness during the impact event.
- Strength design. The ship is supposed to have minor deformation during the impact event.

The design of the ships against various ice loads usually uses the "strength design" principle as this principle ignores the ice deformation and failure. This method may be over-conservative if the ice loads are significant. The "share-energy design" principle is more realistic as it considers the deformations of both the ship and the ice. However, the difficulty of this approach is that the ice deformation (especially the

Table 1
Ice material model parameters [25].

Parameters	Expression	Value	Unit
Density	ρ	900	kg•m^{-3}
Young's modulus	E	9500	MPa
Poisson ratio	ν	0.3	–
Yield function coefficients	a_0	22.93	MPa^2
	a_1	1.06	MPa
	a_2	−0.023	–
Cut-off pressure	p_{cut}	−2	MPa
Initial failure strain	ε_0	0.01	–
Iteration tolerance	TOL	10^{-4}	–

Table 2
Steel properties.

Density (kg/m^3)	Young's modulus (MPa)	Poisson's ratio (-)	Critical strain (1st principal plastic strain) (-)
7850	210,000	0.3	0.15

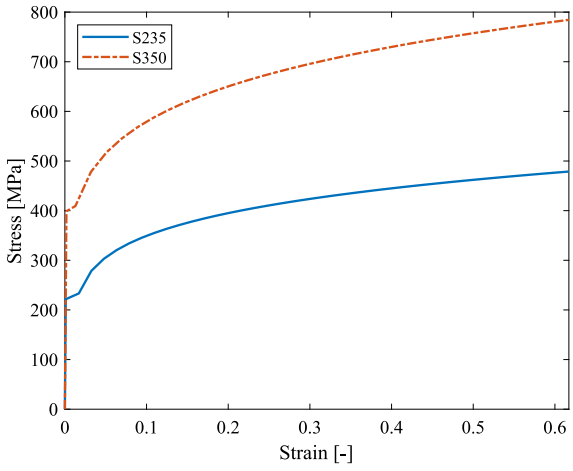

Fig. 2. Stress–strain curves for S235 and S355 steel.

failure modes) is not easy to obtain. This study adopts the "shared-energy design" principle, and a user-defined ice material is used to simulate the ice loads. The surrounding water during the sliding event is ignored because this study focuses only on local deformations of the ice floe and the hull structure. It can be argued that the impact force is relatively small compared to the inertia forces of ship and iceberg, so the relative motions may not change. Moreover, such simplification reduces the computation demands significantly.

In the present study, Abaqus/Explicit is used as the nonlinear finite element solver [51]. It has been widely used to handle large nonlinear systems, including contacts and plastic material behaviours.

2.1. Simulation of ice failure

Simulating the ice failure behaviours is crucial in this numerical study. In addition to the rigid representation of ice, we adopted the plasticity-based material model by Liu et al. [27], extensively used in ice-related studies. The main parameters are summarized in this section.

Derradji-Aouat [42] proposed a unified failure envelope for isotropic freshwater ice and iceberg ice, which can be further written as the following equation (Tsai-Wu yield function):

$$f(p, J_2) = J_2 - (a_0 + a_1 p + a_2 p^2) \tag{1}$$

where p (MPa), the hydrostatic pressure, equals to $-\frac{1}{3}(\sigma_{11} + \sigma_{22} + \sigma_{33})$; J_2 (MPa^2) is the second invariant of stress tensor; the coefficients a_0, a_1, a_2 are constants derived from the experimental data.

The Tsai-Wu yield criterion and the associated flow rule decide the trajectory of the stress state. A failure criterion determines when the flow of stress will end, in other words, the onset of failure. If the equivalent plastic strain grows larger than the failure strain, the element fails and should be deleted. Besides, the hydrostatic pressure will not exceed cut-off pressure. The expressions are written as Eq. (2), where $\varepsilon_{p,eq}$ and ε_f are the equivalent plastic strain and failure strain, and their formulae are presented as Eq. (3); p is the hydrostatic pressure; p_{cut} is the cut-off pressure.

$$\begin{aligned} &\text{if} \quad \varepsilon_{p,eq} > \varepsilon_f\,, \quad \text{delete element} \\ &\text{or} \\ &\text{if} \quad p < p_{cut}, \quad p = p_{cut} \text{ and } \sigma_{11} = \sigma_{22} = \sigma_{33} = -p_{cut} \end{aligned} \tag{2}$$

$$\begin{aligned} \varepsilon_{p,eq} &= \sqrt{\frac{2}{3}\boldsymbol{\varepsilon}_p : \boldsymbol{\varepsilon}_p} \\ \varepsilon_f &= \varepsilon_0 + \left(\frac{p}{p_2} - 0.5\right)^2 \end{aligned} \tag{3}$$

where $\boldsymbol{\varepsilon}_p$ is the plastic strain; ε_0 is the initial failure strain, defined according to experimental data; p_2 is the larger root of the yield function.

In the yield criterion and failure criterion, the constant input values are a_0, a_1, a_2, ε_0, and p_{cut}, whose values are shown in Table 1.

In the present study, this material is implemented in ABAQUS by the user-defined routine, VUMAT. The details about the implementation can be seen in Appendix A. It is noted that the real stress and strain in the implementation are calculated by the Newton-Raphson iteration method. It is thus straightforward to include anisotropic ice yield functions.

Validation tests are performed to ensure the validity of the material model. The detailed results are included in Appendix B and C. In Appendix B, structure-ice compression simulations are performed, and the contact pressure-area relationships obtained from the simulations agree well with the ISO design curve [53]. In Appendix C, the developed ice material model is validated against the results of the ice compressive test by Kim et al. [54] and the ice drop test by Ince et al. (2017b) [21]. For moving ice load cases, comparison between the test results from Quinton [5] and the corresponding simulation results are included in Appendix D; good agreement are obtained. The implemented ice material model has simple inputs which can be obtained through physical tests and also with acceptable computational stabilities and efficiencies. Consequently, it is considered as a suitable ice model for performing detailed ice-structure interaction simulations.

2.2. Simulation of steel failure

The embedded steel model in Abaqus, including the plastic hardening and the ductile damage, is applied to the ship structure. The equivalent plastic strain at the onset of failure is set as the 1st principal plastic strain based on the recommendation from DNV-RP-C208 [55]. It can be further converted to the triaxiality-based equivalent failure plastic strain. This study does not consider the strain rate effects during the impacts as the impact velocity is relatively low. A linear damage evolution rule is used to model the material damage development, and the displacement at failure is defined as critical strain times the characteristic mesh size. The detailed discussions can be found in Liu [56]. The critical failure strain shall be calibrated with the experimental tests for the ship steel; however, the simplification of steel failure will not influence the main conclusions of this study. The material properties, including the critical strain of hull structures, are provided in Table 2. The stress and strain curves for S235 and S350 materials used in the simulations are shown in Fig. 2.

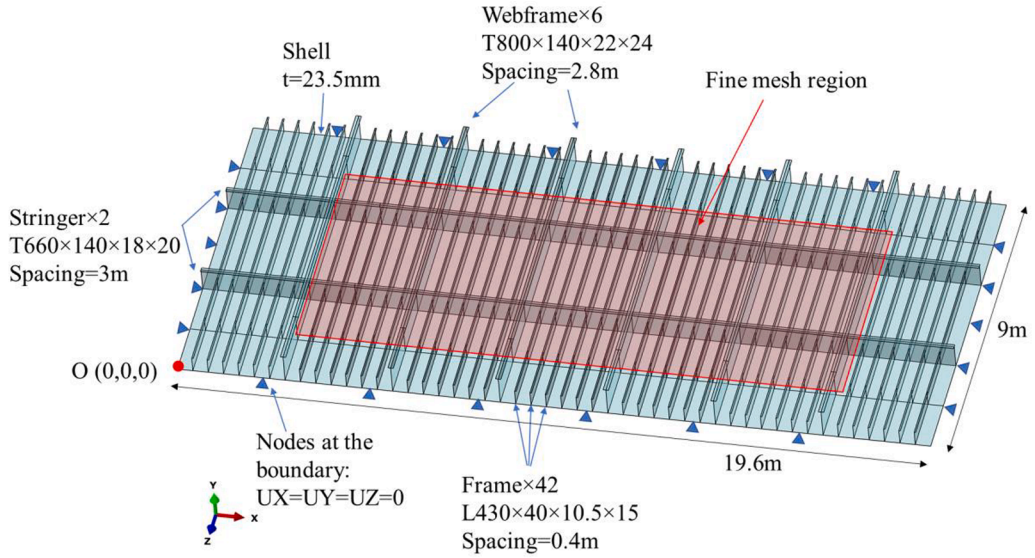

Fig. 3. Stiffened plate geometry model [57].

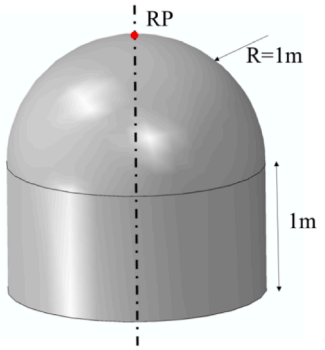

Fig. 4. The local contact geometry of the ice floe.

3. Numerical models for sliding impacts

3.1. Geometry model and mesh

The numerical model of the hull structures is defined as a stiffened plate shown in Fig. 3. The dimensions of the numerical model are based on the ship M/T Uikku [57], designed according to the FSICR IA Super class [52]. The plating model consists of a shell plate, two stringers, six web frames, and 42 frames. It is meshed with shell element S4R [51], and the average mesh size is 50 mm in the contact area. The origin of the reference frame is point O at the bottom-left corner. The four edges are simply supported. The ice floe is modelled as a combination of a sphere and a cylinder, given in Fig. 4. The mesh size of the ice floe is 50 mm × 50 mm × 50 mm. This mesh size is selected based on the mesh size sensitivity analysis in Appendix B.

3.2. Material model

The VUMAT user subroutine for ice material (see Appendix A and Section 2) is used to simulate ice sliding loads. The ice floe is also considered a rigid body for comparison to investigate the effect of ice material stiffness on the local responses of the hull. Steel S235 and steel S350 are chosen as the stiffened plate's material, which simulates the relatively 'weak' (non-ice-classed ship) and 'strong' (ice-classed ship) stiffness, respectively. The stress–strain relationships of steel S235 and S350 are shown in Fig. 2.

3.3. Boundary conditions and sliding/moving loads using a spherical ice floe

All the nodes on the boundary of the stiffened plate are constrained in all transitional directions. The sliding of the ice floe is simulated by prescribed displacements on both x- and y-directions. Prescribed displacements are presented as a smooth normalized displacement curve in Fig. 5, where the magnitudes in x- and y-directions are 11200 mm and 1000 mm, respectively. The starting position of the ice floe's reference point locates at (4200, 0, 4500) mm. The sliding motion is illustrated in Fig. 6.

In the stationary load cases, the impact location on the stiffened plate is (9800, 0, 4500) mm, which is also the starting location of the ice floe's reference point. The penetration depth is ranging from 0 to 1000 mm. The vertical loading condition is the same as sliding load cases.

3.4. Load cases

The variables for sliding load simulations are the ice material type, the steel material type, and the friction coefficient. In total, eight load cases are proposed and listed in Table 3.

Two steel materials will be used in the stationary load cases, i.e., S235 and S350. The stationary load cases are presented in Table 4.

4. Results and discussion

Structural responses of the stiffened plate subjected to sliding ice loads are presented in following sections. Effects of the friction coefficient, the ice material, and the steel material are analysed. The hull's contact force and energy partition are discussed throughout the sliding loading process. Total sliding distances (in the x- and y-axes) are the same in each sliding case.

4.1. Effect of friction coefficient

Contact forces in x- (tangential) and y- (normal) directions and the maximum deflection throughout loading processes are extracted from simulations. Fig. 7 presents the relationship between the total friction coefficient and the maximum deflection in the load cases LC1 to LC4, where the total friction coefficient is defined as the ratio of the contact force in the x-direction (F_x) to the contact force in the y-direction (F_y), which is F_x/F_y. Results of LC1 and LC3 show that the total friction can be larger than zero even though the static structure-to-structure friction

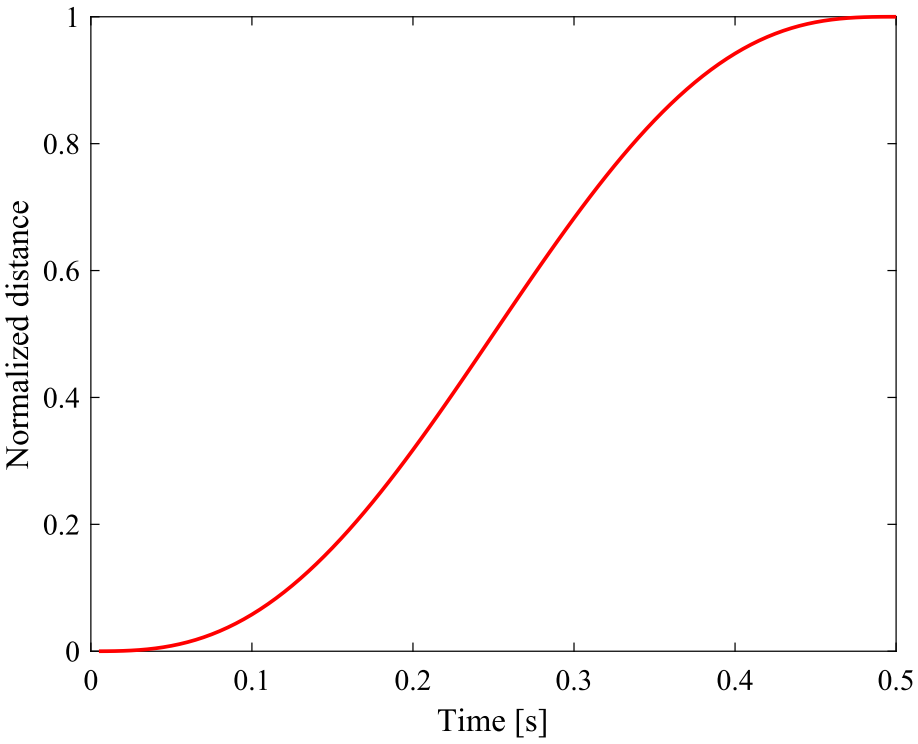

Fig. 5. Normalized displacement of the ice floe's reference point.

coefficient μ is set as zero. This phenomenon means that the deformation and failure of the ice floe and the hull structures can also contribute to the friction. Moreover, vertical distances between curves of $\mu = 0$ (LC1 and LC3) and curves of $\mu = 0.15$ (LC2 and LC4) are around 0.15. Therefore, the total friction might be considered as the superposition of the static structure-to-structure friction and the dynamic friction due to the structural deformation. By comparing the results of the elastic–-plastic ice material (LC1 and LC2) and the rigid ice (LC3 and LC4), the static friction coefficient has different influences on the hull structure's local responses. The total friction becomes larger with a larger static friction coefficient for both ice models. A larger static friction coefficient for the elastic–plastic ice model will induce a much larger hull deflection. However, the static friction coefficient does not significantly affect the hull deflection when the ice floe is considered a rigid body since two curves (LC3 and LC4) have similar patterns. The impact of a rigid ice floe can cause a much larger hull deflection than an elastic–plastic ice floe, as the hull structure dissipates all the impact energy. Fig. 8 shows the simulation screenshots at the final step of LC2 and LC4.

In addition to the hull deflection and contact forces, the static friction coefficient also influences the hull's energy partition. This section analyses the hull's normalized energy (internal energy or plastic dissipated energy). The internal energy is the sum of the recoverable elastic strain energy and the energy dissipated though inelastic processes such as plasticity. Note that the frictional dissipated energy is not included as part of the internal energy (see [51] and Appendix A for details. As shown in Fig. 9 (the case of the elastic–plastic ice model), the hull's normalized internal energy, R_{in}, and the normalized plastic dissipated energy, R_{pd}, increase with the increase of the static friction coefficient μ, which means that more internal energy and plastic dissipated energy is distributed to the hull. The normalized energies are obtained from Eq. (4) and Eq. (5).

$$R_{\text{in}} = E_{\text{in,h}}/E_{\text{in,t}} \tag{4}$$

$$R_{\text{pd}} = E_{\text{pd,h}}/E_{\text{pd,t}} \tag{5}$$

where R_{in} and R_{pd} are the hull's normalized internal and plastic dissipated energy; $E_{\text{in,h}}$ and $E_{\text{pd,h}}$ are the hull's internal energy and plastic dissipated energy; $E_{\text{in,t}}$ and $E_{\text{pd,t}}$ are the total internal energy and plastic dissipated energy during the impact event, and "total" means the sum of the hull's and the ice floe's energy. When the ice floe is a rigid body, all the energy is distributed to the hull structures, consequently $R_{\text{in}} = R_{\text{pd}} = 1$. Note that Eqs. (4) and (5) consider only the internal energy of the system (hull and ice).

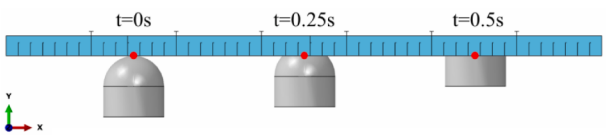

Fig. 6. Sliding load condition.

Table 3
Load cases (moving).

Load case	Ice material	Steel material	Friction coefficient
LC1	VUMAT for ice	S235	0
LC2	VUMAT for ice	S235	0.15
LC3	Rigid body	S235	0
LC4	Rigid body	S235	0.15
LC5	VUMAT for ice	S350	0
LC6	VUMAT for ice	S350	0.15
LC7	Rigid body	S350	0
LC8	Rigid body	S350	0.15

Table 4
Load cases (stationary).

Load case	Ice material	Steel material	Friction coefficient
LC9	VUMAT for ice	S235	0.15
LC10	VUMAT for ice	S350	0.15

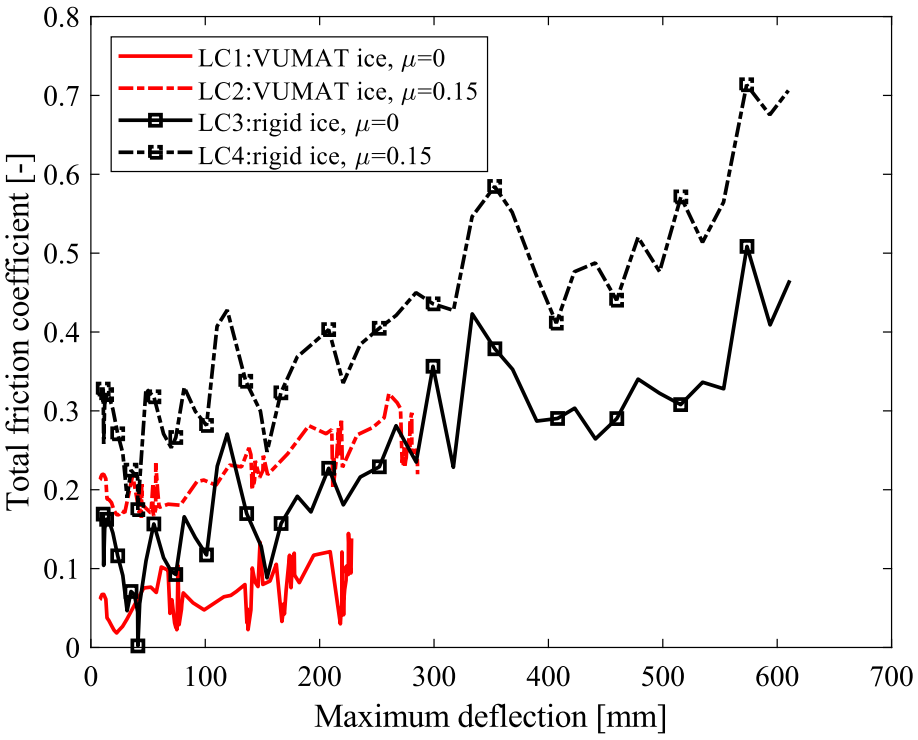

Fig. 7. Total friction coefficient versus the maximum deflection of the hull (LC1, LC2, LC3, LC4).

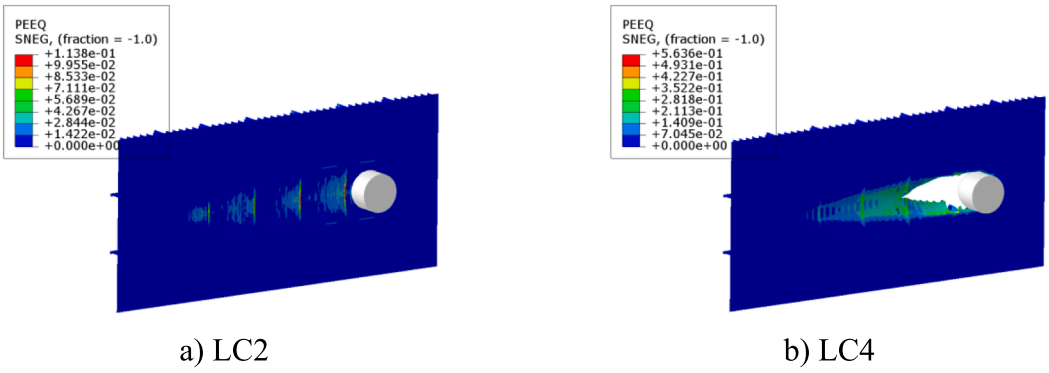

Fig. 8. Screenshots of LC2 and LC4 at final simulation stages.

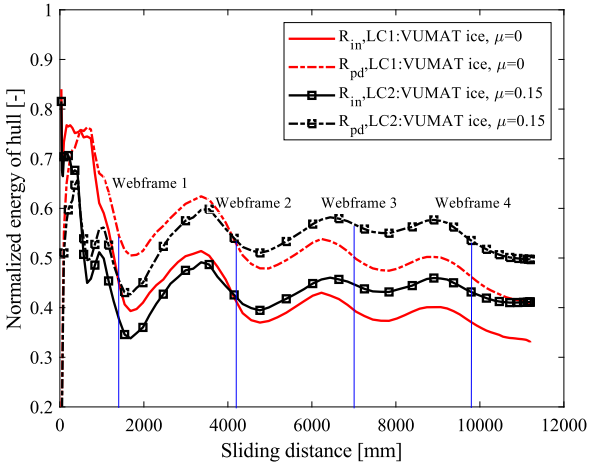

Fig. 9. The normalized energy of the hull (LC1, LC2) with the location of web frame annotated.

4.2. *Effect of ice material*

As mentioned in Section 4.1, the hull's deflection is much larger when subjected to the impact of a rigid ice floe than an elastic–plastic ice floe, according to the comparisons in S235 steel cases. In this section, the effect of ice material on the hull's deflection is also discussed in S350 cases. Maximum deflections for load cases LC2, LC4, LC6, and LC8 are given in Fig. 10. Hull's maximum deflections rise and fluctuate periodically with the sliding distance of the ice floe for the VUMAT ice material. For cases of rigid ice (LC4 and LC8), maximum deflections are significantly higher than elastic–plastic ice floe cases (LC2 and LC6), and maximum deflections are nearly proportional to the sliding distance before the hull begins to fail. Hull deflection curves for two steel materials (S235 and S350) almost overlap when the ice is rigid. Simulation screenshots at the final step of LC4 and LC8 are shown in Fig. 11.

Contact forces in x- and y-directions are given in Fig. 12 and Fig. 13. For both steel materials, friction force curves (the contact force in the x-direction) in cases of the elastic–plastic ice floe and the rigid ice floe nearly overlap within the same deflection range. Still, vertical force

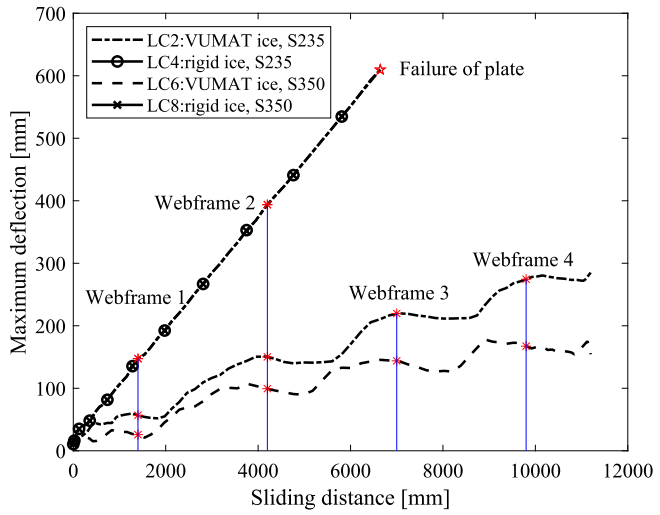

Fig. 10. Maximum deflection versus sliding distance (LC2, LC4, LC6, LC8) with the location of web frame annotated.

curves (the contact force in the y-direction) are much higher in the case of the elastic–plastic ice floe than in the case of the rigid ice floe. Thus, the ice material model mainly influences the vertical contact forces and has few effects on friction forces. This phenomenon can be explained by the increased contact area between the hull and the ice floe when the elastic–plastic ice material model is employed.

Fig. 14 and Fig. 15 show that the normalized internal energy and plastic dissipated energy equal to one when the ice floe is considered a rigid body for the load case LC4 and LC8. It means that all energies will be allocated to the hull in this condition. However, normalized energies are less than one and fluctuate with sliding distance when the VUMAT user subroutine is adopted (LC2 and LC6). The hull's normalized plastic dissipated energy seems to converge to a value of 0.5 in this case. A rigid ice representation may overestimate impact loads significantly.

4.3. *Effect of structural stiffness*

The total friction coefficient, i.e., the ratio of the tangential contact force (x-direction) to the vertical contact force (y-direction), is investigated in this section to study the effect of steel material, i.e., an alternative way to study influences of different structural stiffness. Fig. 16 shows the total friction coefficient versus maximum hull deflection in the load cases LC2 and LC6. It is observed that the final deflection of the S235 hull is almost twice the deflection of the S350 hull and the total friction for the S235 case is larger than the S350 case. When the hull's strength is higher, the relative deformation in the contact zone is smaller. Thus, the total friction decreases.

The energy partition has different patterns when different steel materials are adopted. Fig. 17 shows that more energies (internal energy and plastic dissipated energy) are distributed to the hull in the S235 case

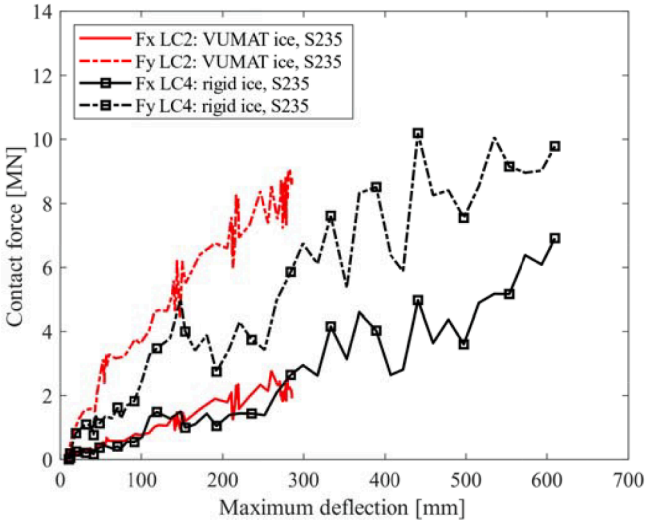

Fig. 12. Contact forces in the x- and y-direction versus the maximum deflection (LC2, LC4).

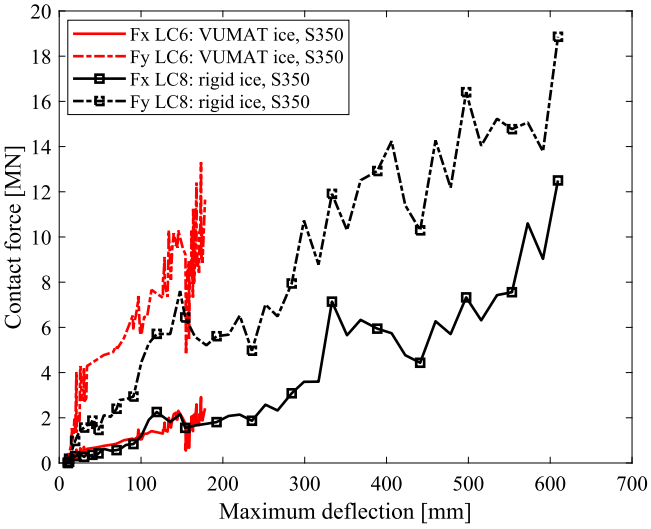

Fig. 13. Contact forces in the x- and y-direction versus the maximum deflection (LC6, LC8).

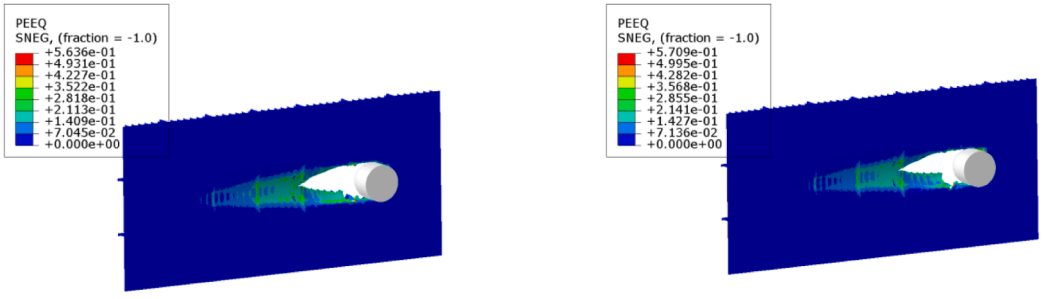

a) LC4 b) LC8

Fig. 11. Screenshots of LC4 and LC8 at final simulation stages.

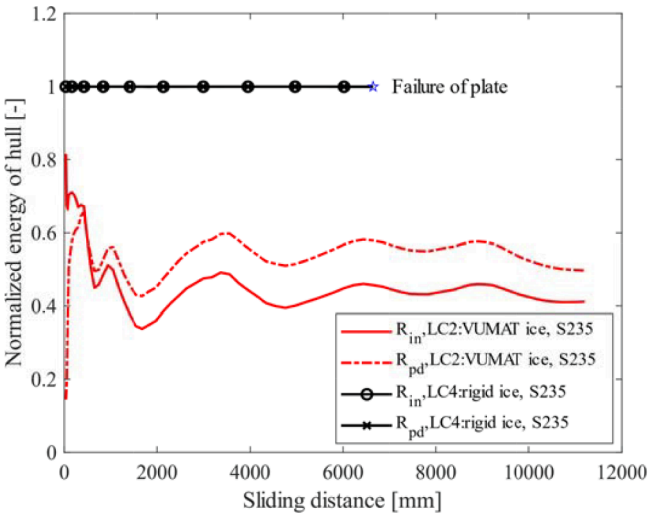

Fig. 14. The normalized energy of the hull (LC2, LC4).

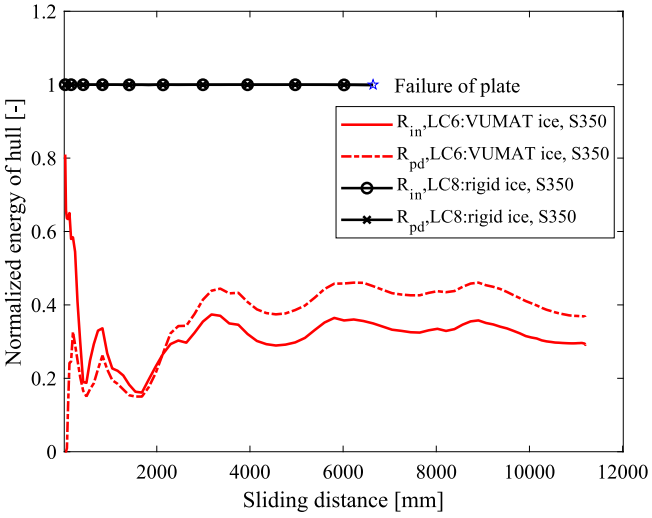

Fig. 15. The normalized energy of the hull (LC6, LC8).

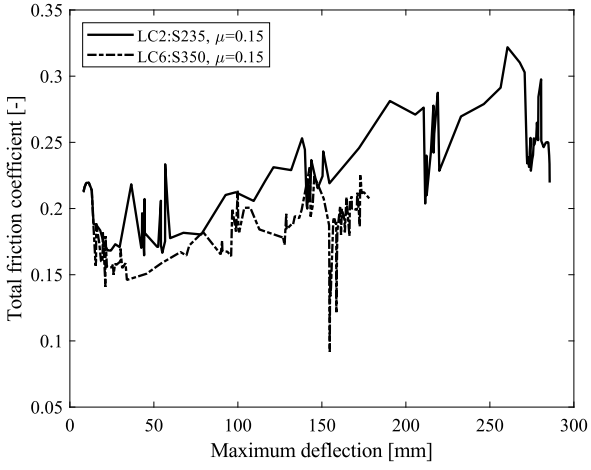

Fig. 16. Total friction coefficient versus the maximum deflection of the hull (LC2, LC6).

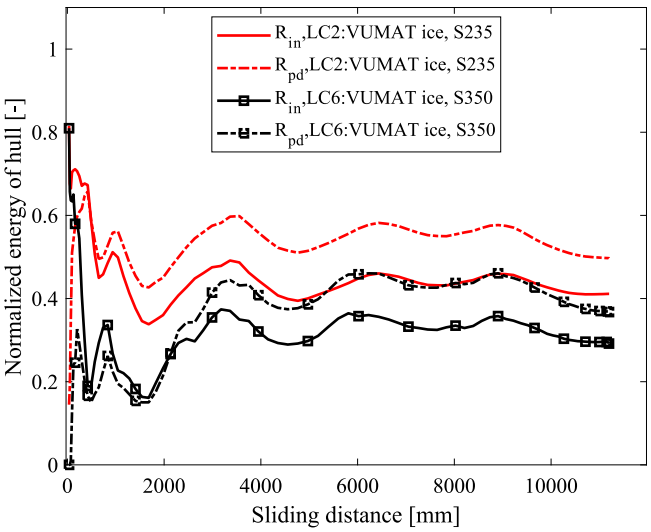

Fig. 17. The normalized energy of the hull (LC2, LC6).

than in the S350 case. This phenomenon involves more severe deflection and larger friction when the hull's strength is lower (i.e., the non-ice classed ship). Screenshots of LC2 and LC6 at the final simulation stage are presented in Fig. 18.

4.4. Stationary load condition

In this section, the stationary impact of the ice floe on the hull is simulated to compare its load pattern with the sliding load cases. Contact forces in the penetration direction and maximum deflections in load cases LC2, LC6, LC9 and LC10 are shown in Fig. 19.

For stationary load cases LC9 and LC10, contact forces for the S235 hull keep rising with the increase of maximum deflection and start to drop when the failure of the shell plate starts. However, the contact force for the S350 hull increases with large fluctuations. This phenomenon can be explained by different deformation and failure patterns of the ice floe. Interactions between ice floes and the hull at the end of the simulation (t = 0.5 s, the penetration distance = 1000 mm) are presented in Fig. 20. For the S235 steel case, the larger deflection of the hull's shell plate causes the ice floe to be more confined by the shell plate, making the ice floe more rigid and thus more difficult to fail. Therefore, no obvious loading and unloading of the contact force are observed in the S235 steel case. In the S350 steel case, the ice floe is less confined, and many ice elements on the top of the ice floe are eroded (Fig. 20 b)), which leads to a larger contact area between the hull and the ice. Thus, within the same range of the hull's deflection, the contact force in the S350 case is greater than the S235 case. Moreover, the deletion of ice elements also causes fluctuations of contact force in the S350 case.

The comparison between vertical contact forces in sliding and stationary load cases is also shown in Fig. 19. Under the same maximum hull deflection, contact forces in sliding load cases are larger than corresponding stationary load cases. It is probably due to the increased contact areas during the sliding process if the ice deformation and failure are considered. This observation might differ if a rigid body is used to represent the ice.

5. Conclusion

The present work performs numerical simulations of an ice floe sliding along a hull structure. A numerical framework has been shown, which can be used for the hull structure design by considering the impact of moving ice features. A VUMAT user subroutine for ice material has been implemented in ABAQUS successfully. Sensitivity studies have been performed using different ice and steel materials and friction

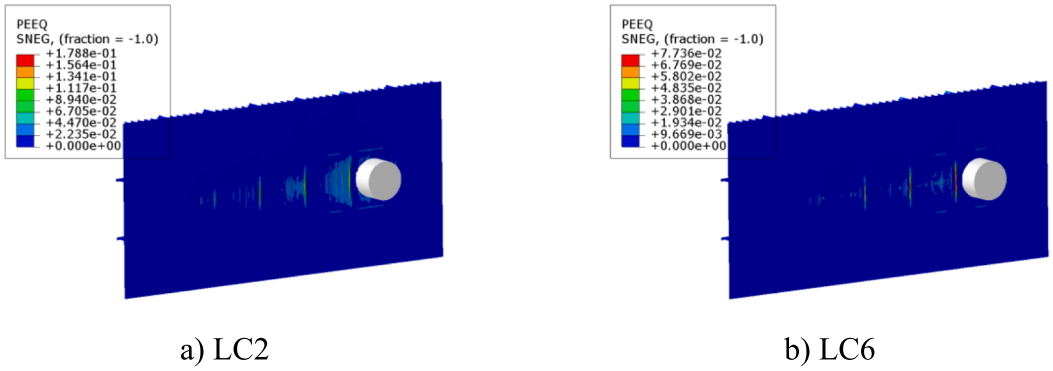

Fig. 18. Screenshots of LC2 and LC6 at final simulation stages.

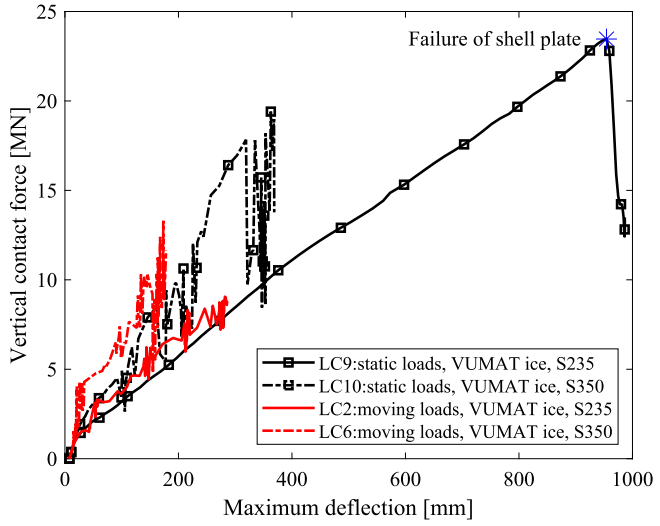

Fig. 19. Vertical contact forces versus the maximum deflection (LC2, LC6, LC9, LC10).

factors.

The main results are summarized as follows:

(1) Effects of the static friction coefficient and the structures' local deformation contribute to the total friction during the sliding process. The increase of the static friction coefficient causes the increase of the total friction, the increase of the hull's deflection, and more energy (internal energy and plastic dissipated energy) distributed to the hull structures.
(2) When the ice floe is considered as a rigid body, the static friction coefficient has little influence on the local structural responses of the hull. Only the hull deformation contributes to the total friction, and all energies are allocated to the hull structures.
(3) By comparing contact forces in the sliding load cases with different ice material models, friction forces, which are contact forces in the x-direction, are almost the same when the same deflection is caused to the hull. However, normal contact forces in the case of the elastic–plastic ice material are larger than in the case of the rigid ice due to the larger contact area caused by the failure of ice. This can be only observed when using deformable ice material models.
(4) The structural stiffness of the hull structures also influences local structural responses. When the hull's strength increases (for example, from non-ice-classed ships to the ice-classed ships), the hull deflection, the total friction, and the energy dissipation of the hull decrease.
(5) The effect of the hull structural stiffness on local structural responses is more significant in stationary load cases than in sliding load cases. Different ice failure patterns are observed in stationary load cases when the hull has different structural stiffness. When the structural stiffness of the hull is lower, the ice floe is more constrained and more difficult to fail in this case. Among the sliding load cases, the failure patterns of the ice floe are similar with different stiffness of the hull structure.
(6) Simulation results show that the hull's contact forces and deflection at final stages in stationary load cases are greater than in sliding load cases if the same prescribed normal displacement is applied to the ice floes. However, when the same deflection of the hull is caused, the contact forces in moving load cases are larger than in stationary load cases if the ice is deformable. In other words, it might be not conservative to use a rigid body to represent moving ice loads.

CRediT authorship contribution statement

Jianan Zhang: Conceptualization, Methodology, Software, Validation, Formal analysis, Investigation, Writing – original draft, Writing – review & editing, Visualization. **Zhenhui Liu:** Conceptualization, Methodology, Formal analysis, Investigation, Writing – review & editing, Supervision. **Muk Chen Ong:** Conceptualization, Formal analysis, Investigation, Writing – review & editing, Resources, Supervision. **Wenyong Tang:** Conceptualization, Investigation, Writing – review & editing.

Declaration of Competing Interest

The authors declare that they have no known competing financial interests or personal relationships that could have appeared to influence the work reported in this paper.

Data availability

Data will be made available on request.

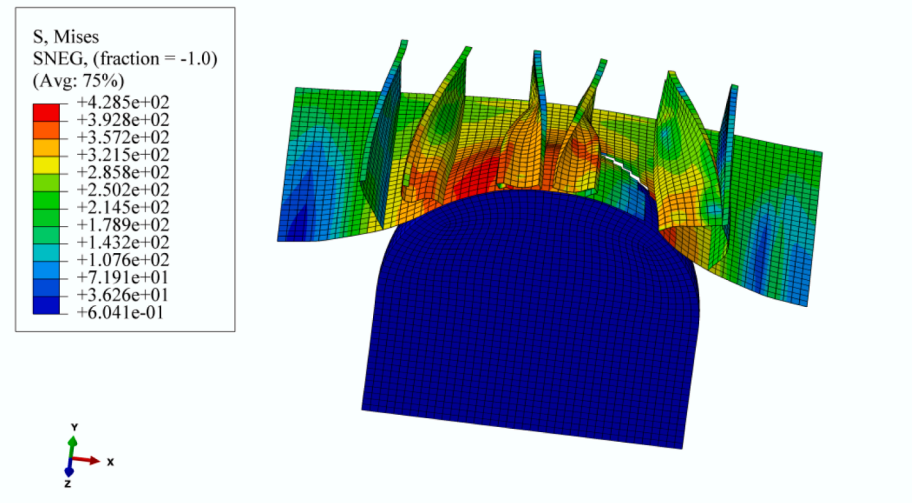

a) S235 hull (LC9)

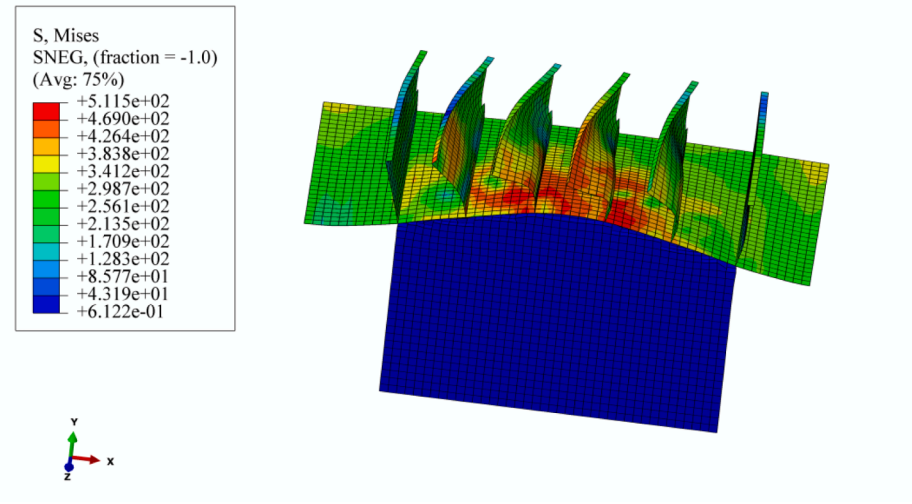

b) S350 hull (LC10)

Fig. 20. Deformation and failure of the ice floe at t = 0.5 s (LC9, LC10).

Appendix A:. Implementation of the VUMAT user subroutine for ice material

The ice material model is incorporated into ABAQUS via the VUMAT user subroutine. Essential components of this subroutine are the elastic–plastic stress/strain update algorithm and the failure criterion (see Table A-1).

At the start of the subroutine, a group of variables of the last increment, $\{\boldsymbol{\sigma}_n, \boldsymbol{\varepsilon}_n, \boldsymbol{\varepsilon}_{p,n}, \Delta\boldsymbol{\varepsilon}\}$, is sent from the main program, where $\boldsymbol{\sigma}_n$ is the stress, $\boldsymbol{\varepsilon}_n$ is the total strain, $\boldsymbol{\varepsilon}_{p,n}$ is the plastic strain, and $\Delta\boldsymbol{\varepsilon}$ is the total strain increment. There are two main steps for updating stress and strain, i.e., the elastic prediction and the plastic correction. The stress state of ice is assumed to be elastic at the beginning, and the trial stress, $\boldsymbol{\sigma}_{trial,n+1}$, is calculated based on the Generalized Hooke's Law, presented in Eq. (A-1) where $\boldsymbol{C}_e$ is the elastic stiffness matrix. If the yield function for trial stress, $f(\boldsymbol{\sigma}_{trial,n+1})$, is negative, the stress state is still at the elastic stage. Otherwise, the stress state transforms into plasticity, and the plastic correction step should be executed. The plastic correction step aims to calculate the real stress and strain which are on the yield surface and obey the associated flow rule. The fully implicit

Table A-1
Variables to be stored.

Variables to be stored	Expression	Unit
Stress	$\boldsymbol{\sigma}_{n+1}$	MPa
Total strain	$\boldsymbol{\varepsilon}_{n+1}$	–
Plastic strain	$\boldsymbol{\varepsilon}_{p,n+1}$	–
Equivalent plastic strain	$\varepsilon_{p,eq}$	–
Failure strain	ε_f	–
Plastic multiplier	$\Delta\lambda_{n+1}$	MPa^{-1}
Hydrostatic pressure	p	MPa
Element deletion controller	Status	–
Internal energy	E_{in}	mJ
Dissipated plastic energy	E_{pl}	mJ

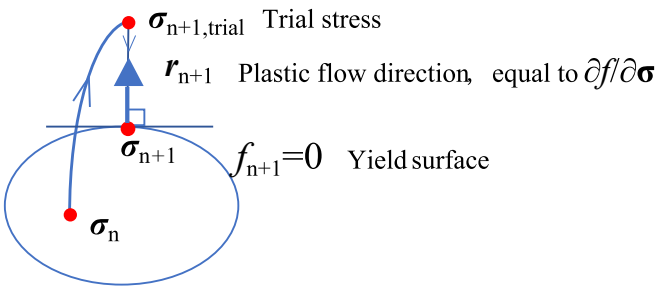

Fig. A-1. Diagram of the stress update algorithm.

backward Euler method is adopted in the plastic correction step to bring the stress back to the yield surface, as shown in Eq. (A-2). $\boldsymbol{\sigma}_{n+1}$, $\boldsymbol{\varepsilon}_{n+1}$, $\boldsymbol{\varepsilon}_{p,n+1}$ are the stress, the total strain, and the plastic strain in the increment n + 1. $\boldsymbol{\varepsilon}_n$ and $\boldsymbol{\varepsilon}_{p,n}$ are the total strain and the plastic strain in the last increment. $\Delta\lambda_{n+1}$ is a plastic multiplier. $\boldsymbol{r}_{n+1}$ represents the flow direction of this increment and equals $\left(\frac{\partial f}{\partial \boldsymbol{\sigma}}\right)_{n+1}$. This algorithm can also be expressed as Fig. A-1.

$$\boldsymbol{\sigma}_{trial,n+1} = \boldsymbol{\sigma}_n + \boldsymbol{C}_e : \Delta\boldsymbol{\varepsilon} \tag{A-1}$$

$$\begin{aligned} &\boldsymbol{\sigma}_{n+1} = \boldsymbol{C}_e : \left(\boldsymbol{\varepsilon}_{n+1} - \boldsymbol{\varepsilon}_{p,n+1}\right) \\ &\boldsymbol{\varepsilon}_{n+1} = \boldsymbol{\varepsilon}_n + \Delta\boldsymbol{\varepsilon} \\ &\boldsymbol{\varepsilon}_{p,n+1} = \boldsymbol{\varepsilon}_{p,n} + \Delta\lambda_{n+1}\boldsymbol{r}_{n+1} \\ &f(\boldsymbol{\sigma}_{n+1}) = 0 \end{aligned} \tag{A-2}$$

The real stress and strain are calculated by Eq. (A-3) with Newton-Raphson iteration. Since the plastic strain can be obtained from the real stress and the plastic multiplier, there are only two unknown variables to be solved, i.e., $\boldsymbol{\sigma}_{n+1}$ and $\Delta\lambda_{n+1}$. The initial value of the stress, $\boldsymbol{\sigma}_{n+1}^{(k=0)}$, is set as the trial stress, $\boldsymbol{\sigma}_{trial,n+1}$; the multiplier, $\Delta\lambda_{n+1}^{(k=0)}$, equals zero at the beginning of the iteration. The formulae of the stress and the plastic multiplier in the iteration are shown in Eq. (A-3) and Eq. (A-4). The Newton-Raphson iteration will end until the yield function is less than the tolerance, *TOL* (defined as 10^{-4}), as shown in Eq. (A-5).

$$\begin{aligned} &\boldsymbol{\sigma}_{n+1}^{(k+1)} = \boldsymbol{\sigma}_{n+1}^{(k)} + \Delta\boldsymbol{\sigma}^{(k)} \\ &\Delta\lambda_{n+1}^{(k+1)} = \Delta\lambda_{n+1}^{(k)} + \delta\lambda^{(k)} \\ &\delta\lambda^{(k)} = \left[\frac{f}{\left(\frac{\partial f}{\partial \boldsymbol{\sigma}}\right)^T : \boldsymbol{A}^{-1} : \frac{\partial f}{\partial \boldsymbol{\sigma}}}\right]_{n+1}^{(k)} \\ &\Delta\boldsymbol{\sigma}^{(k)} = -\delta\lambda^{(k)}\boldsymbol{A}^{-1} : \left(\frac{\partial f}{\partial \boldsymbol{\sigma}}\right)_{n+1}^{(k)} \end{aligned} \tag{A-3}$$

where $\boldsymbol{A}$ can be obtained from Eq. (A-4); f is the yield function; $\boldsymbol{\sigma}$ is the stress.

$$\boldsymbol{A} = \boldsymbol{C}_e^{-1} + \left(\Delta\lambda\frac{\partial^2 f}{\partial \boldsymbol{\sigma}^2}\right)_{n+1}^{(k)} \tag{A-4}$$

$$f\left[\boldsymbol{\sigma}_{n+1}^{(k+1)}\right] < TOL \tag{A-5}$$

After updating the stress and the multiplier, the plastic strain is updated according to the third equation of Eq. (A-2). Then, the failure criterion is executed, as presented in Eq. (2) and Eq. (3). Besides, the internal energy and the dissipated plastic energy are updated, as shown in Eq. (A-6) and Eq. (A-7), respectively.

$$\begin{aligned} E_{in,n+1} &= E_{in,n} + P_{stress,n+1}/\rho \\ P_{stress,n+1} &= \frac{1}{2}\left[\left(\sigma_{11,n} + \sigma_{11,n+1}\right)\Delta\varepsilon_{11} + \left(\sigma_{22,n} + \sigma_{22,n+1}\right)\Delta\varepsilon_{22}\right. \\ &\quad \left. + \left(\sigma_{33,n} + \sigma_{33,n+1}\right)\Delta\varepsilon_{33}\right] + \left(\sigma_{12,n} + \sigma_{22,n+1}\right)\Delta\varepsilon_{12} \\ &\quad + \left(\sigma_{13,n} + \sigma_{13,n+1}\right)\Delta\varepsilon_{13} + \left(\sigma_{23,n} + \sigma_{23,n+1}\right)\Delta\varepsilon_{23} \end{aligned} \tag{A-6}$$

where.
$E_{in,n+1}$,$E_{in,n}$— the internal energy of increment n + 1 and n;
$P_{stress,n+1}$—the stress power of increment n + 1;
ρ—the current density at the material points in the midstep configuration.

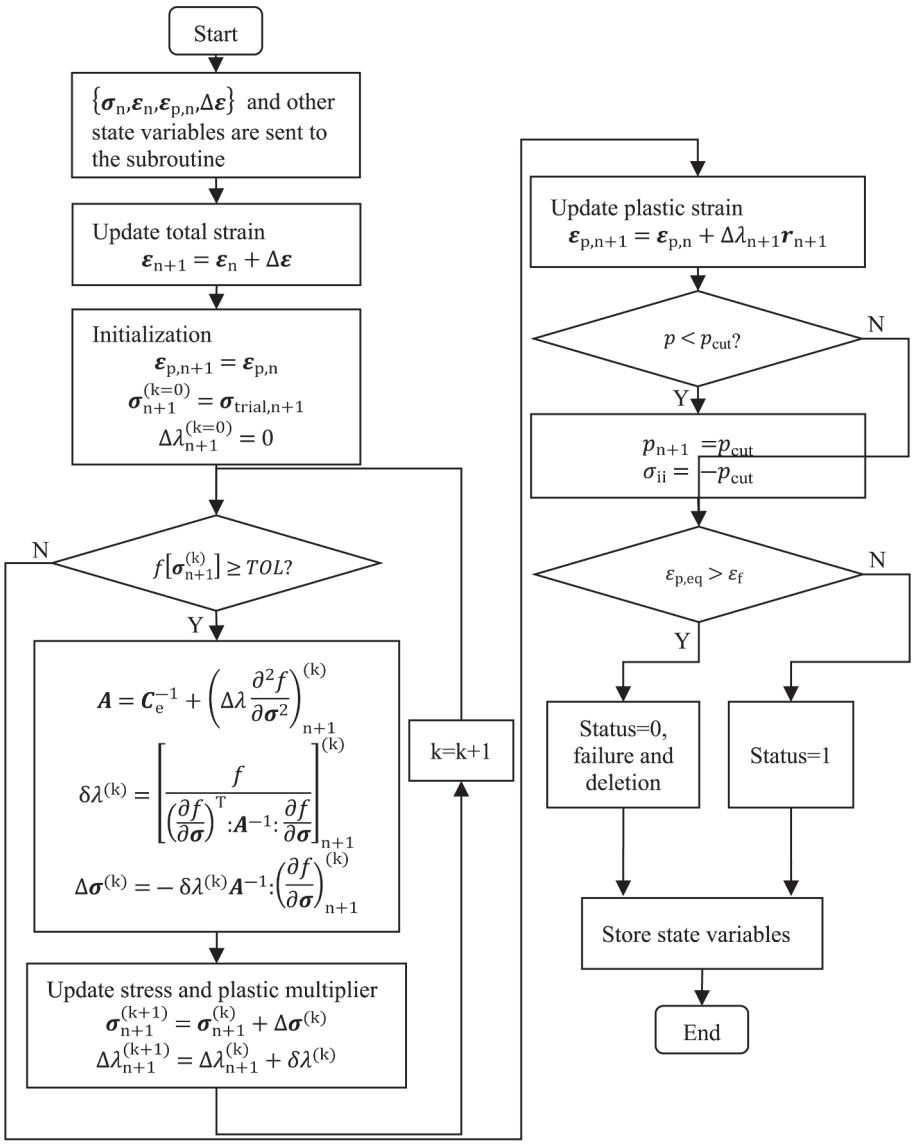

Fig. A-2. The framework of the VUMAT user subroutine.

$$
\begin{aligned}
E_{pl,n+1} &= E_{pl,n} + W_{n+1}/\rho \\
W_{n+1} &= \frac{1}{2}\left[\left(\sigma_{11,n} + \sigma_{11,n+1}\right)\left(\varepsilon_{pl,11,n+1} - \varepsilon_{pl,11,n}\right)\right. \\
&\quad + \left(\sigma_{22,n} + \sigma_{22,n+1}\right)\left(\varepsilon_{pl,22,n+1} - \varepsilon_{pl,22,n}\right) \\
&\quad \left. + \left(\sigma_{33,n} + \sigma_{33,n+1}\right)\left(\varepsilon_{pl,33,n+1} - \varepsilon_{pl,33,n}\right)\right] \\
&\quad + \left(\sigma_{12,n} + \sigma_{22,n+1}\right)\left(\varepsilon_{pl,12,n+1} - \varepsilon_{pl,12,n}\right) \\
&\quad + \left(\sigma_{13,n} + \sigma_{13,n+1}\right)\left(\varepsilon_{pl,13,n+1} - \varepsilon_{pl,13,n}\right) \\
&\quad + \left(\sigma_{23,n} + \sigma_{23,n+1}\right)\left(\varepsilon_{pl,23,n+1} - \varepsilon_{pl,23,n}\right)
\end{aligned}
\tag{A-7}
$$

where.

$E_{pl,n+1}, E_{pl,n}$—the plastic dissipated energy of increment n + 1 and n;

W_{n+1}—the plastic work increment of increment n + 1.

The last step of the subroutine is to store the updated variables listed in Table A-1, and these variables will be sent back to ABAQUS main program for the next increment.

The framework of this VUMAT user subroutine is presented in Fig. A-2. The input parameters of this ice material model are summarized in Table 1 (Section 2.1).

Appendix B:. Validation against the pressure-area relationship

This section performs simulations of ice floes of three shapes colliding with rigid structures. Contact pressure-area relationships are obtained in the

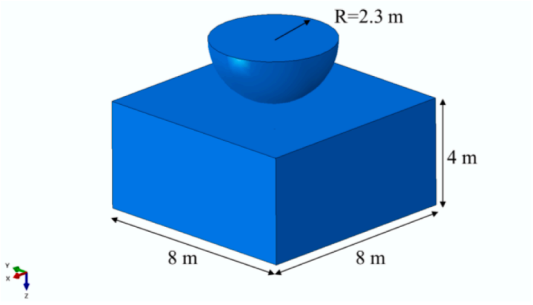

a) A rigid spherical indenter colliding with an ice block

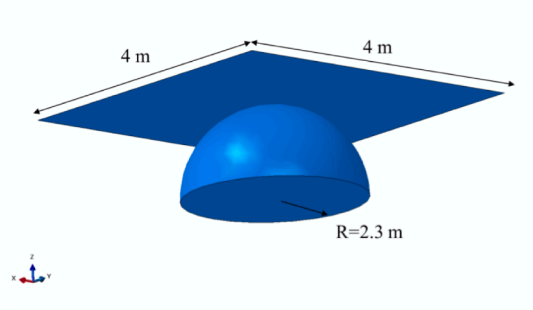

b) A rigid plate colliding with an ice sphere

Fig. B-1. Validation cases a) and b).

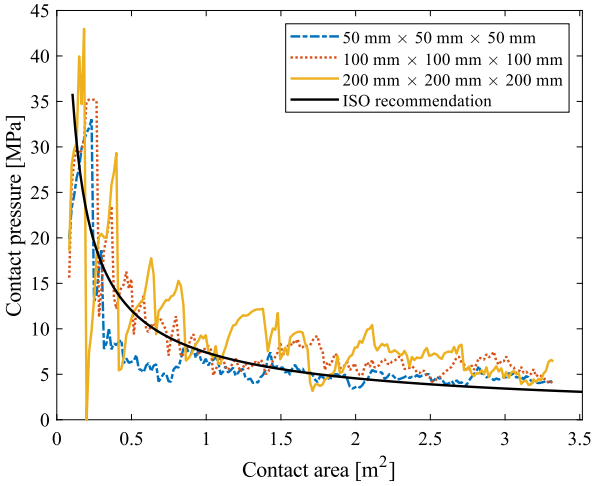

a) A rigid spherical indenter colliding with an ice block

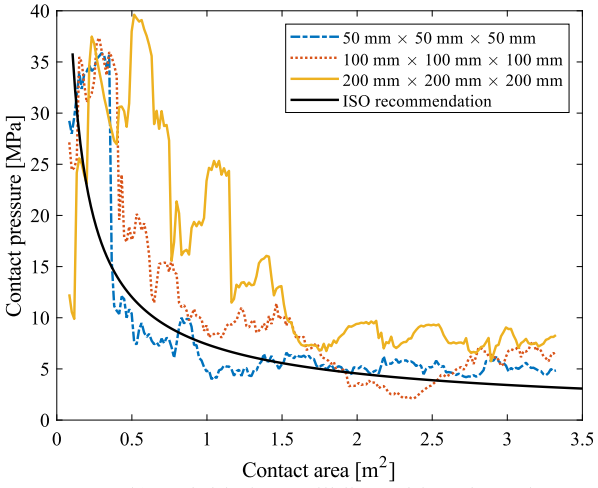

b) A rigid plate colliding with an ice sphere

Fig. B-2. Contact pressure-area relationship curves in the validation case a) and b).

structure-ice compression simulations and agree well with the ISO design curve [53]. Contact forces are also compared with experimental data from test results in Kim et al. [54] and in Ince et al. (2017b) [19] presented in Appendix C.

The ice contact pressure-area relationship of $p = 7.4A^{-0.7}$(MPa) [53] is adopted for comparison as it is often used for the structure design. Two simulation cases are considered as presented in Fig. B-1: a) a rigid spherical indenter colliding with an ice block; b) a rigid plate colliding with an ice sphere. The contact pressure is calculated by the contact force divided by the nominal contact area. The nominal contact area is calculated according to the penetration distance of the rigid indenters. The final penetration distance of the indenters is 230 mm, and the simulation time is 0.5 s. The

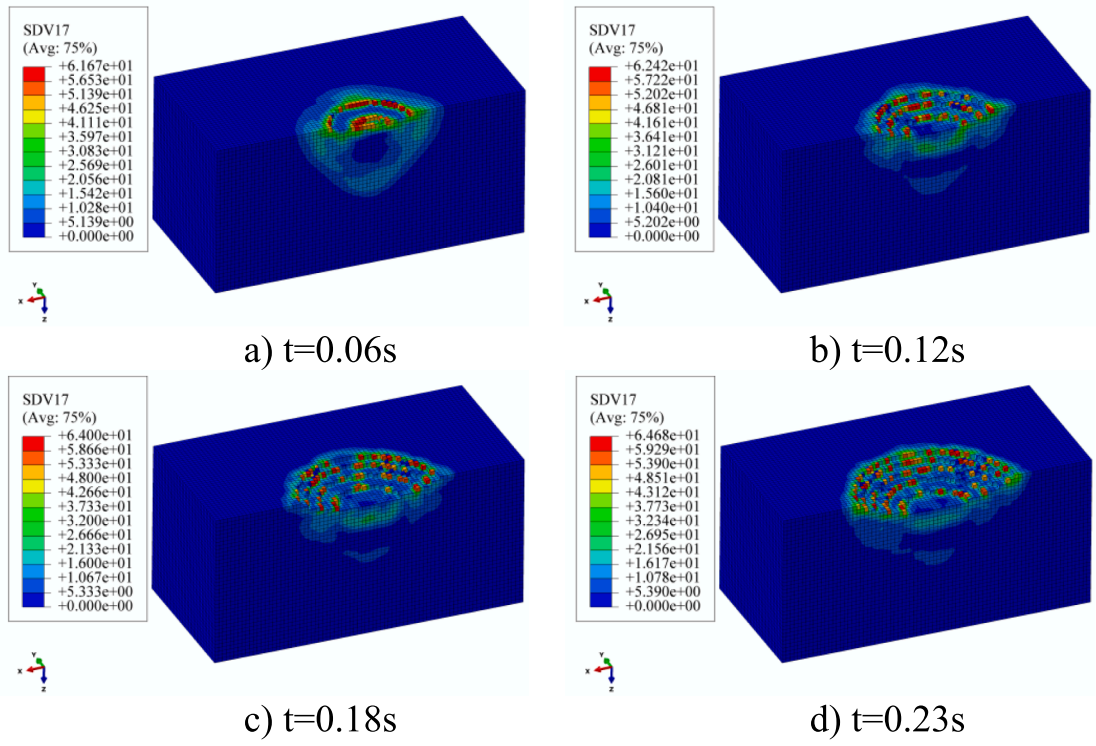

Fig. B-3. Crushing and failure of the ice block (Validation a)).

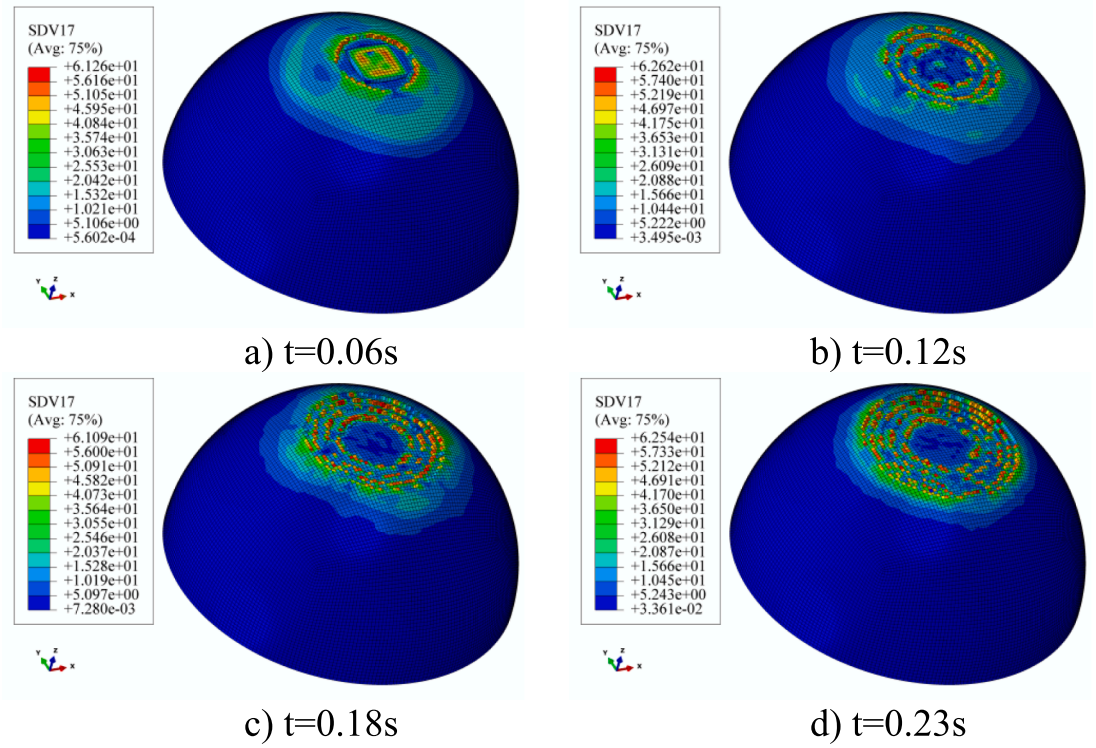

Fig. B-4. Crushing and failure of the ice ball (Validation b)).

interaction between rigid indenters and ice elements is modelled using the general contact algorithm with a friction coefficient of 0.15. Three mesh sizes in the ice-indenter contact zone are employed for mesh size sensitivity analysis: 50 mm × 50 mm × 50 mm, 100 mm × 100 mm × 100 mm, and 200 mm × 200 mm × 200 mm. Fig. B-2 shows that a finer mesh results in a better agreement between simulation curves and the ISO design curve. Therefore, the mesh size 50 mm × 50 mm × 50 mm is recommended in ice-structure interaction simulations in the present study. Ice crushing and failure evolutions at the mesh size 50 mm × 50 mm × 50 mm are provided in Fig. B-3 and Fig. B-4.

Appendix C:. Validation against experimental data

(1) Case 1.

The VUMAT user subroutine developed in this study is also validated against Kim et al.'s laboratory-scale ice compressive test results [54]. The same ice properties are used since no data are available from the tests. The ice specimen was a cone with a 100 mm diameter and a 30 degrees cone angle. The test speed was 1000 mm/s. Fig. C-1 shows the numerical model of this case. The comparison results of total force versus penetration distance are presented in Fig. C-2, including results of three mesh sizes: 2 mm × 2 mm × 2 mm, 3 mm × 3 mm × 3 mm, and 5 mm × 5 mm × 5 mm. As shown in Fig. C-2, the results of three mesh sizes are close to each other, and the simulations agree well with the results from the penetration distance 0 mm to 18 mm. After 18 mm, the test force-distance curve drops suddenly and rises again, while the curves from the simulations keep rising. Nevertheless, the simulation has well captured the trends of the impact force in the test, considering the unknown properties of the ice sample. The failure evolution of the ice is also presented in Fig. C-2.

(2) Case 2.

This VUMAT subroutine is further validated against the ice drop experiment by Ince et al. [19]. A cone-shaped ice indenter (diameter: 0.8 m, height:0.392 m) which is made of freshwater ice is dropped on a steel plate (1.2 m × 1.2 m × 2.9 mm) from a height of 2 m. The experiment setup is shown in Fig. C-3. In the numerical simulation, we use the developed VUMAT subroutine as ice material model since the ice parameters in the test are not compatible to our model. Two steel materials are adopted, i.e., S235 and S350, as described in Section 2.2. We followed the same procedures in our study in the simulation of this test. The movement of the ice cone is simulated by a prescribed displacement.

The contact force and displacement of the ice cone obtained from the numerical simulation are compared with the corresponding results from the experiment, shown in Fig. C-4. The contact force recorded in the experiment is higher than in the simulations; however, these results are in the same quantity range, i.e., the maximum contact forces in the experiment and the simulations are 67.89 kN, 48.57 kN, and 61.90 kN, respectively.

The difference between experimental and numerical results may be reasonable because the ice material properties used in the simulation are different from those in the experiment. The ice material model developed in this paper is used for multi-year sea ice, while the ice specimen in the experiment is made of freshwater ice which is frozen for 24 h. We think that the ice material in this paper is more rigid than the ice made in the experiment. That is why the experimental result curve is higher than the numerical result curves since larger contact area obtained due to the crush of ice in the tests. Moreover, the definition of 'displacement' in this validation might differ from that in the experiment, which may also contribute to the uncertainties.

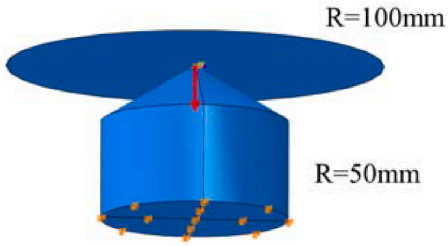

Fig. C-1. Ice cone compression numerical simulation model.

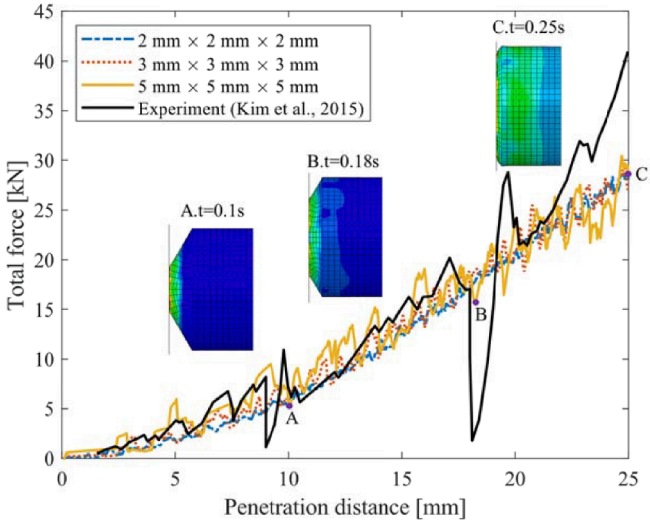

Fig. C-2. Total force versus penetration distance curves (case 1).

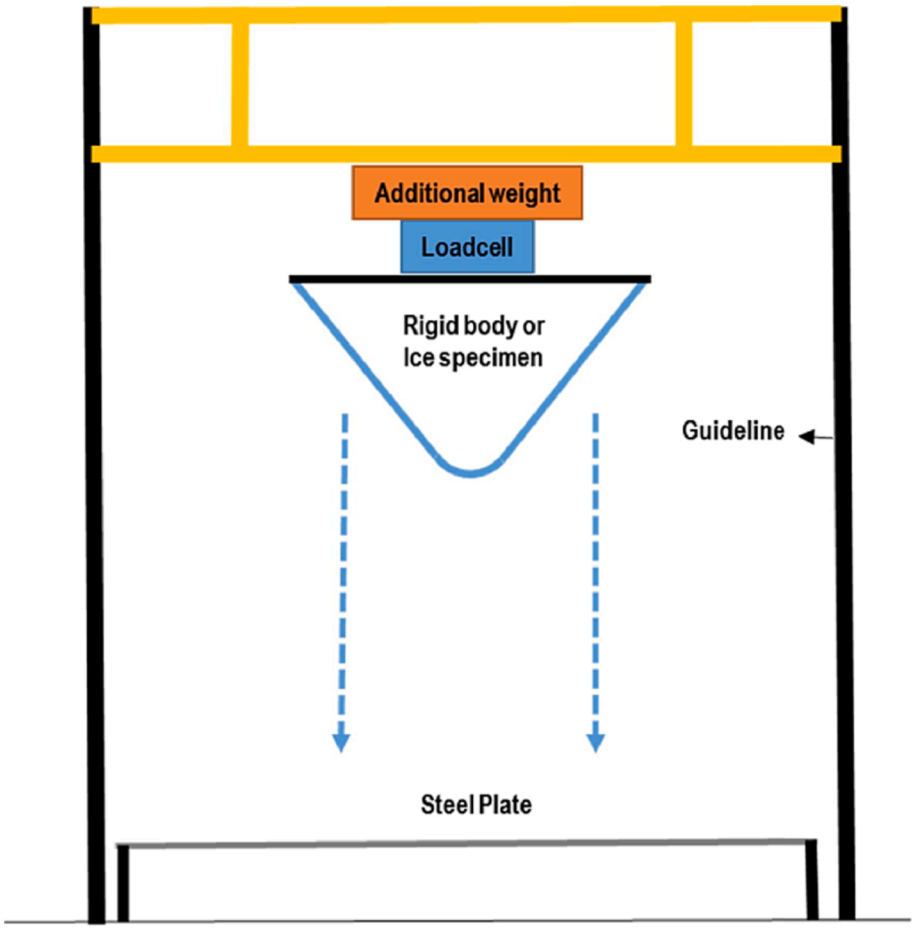

Fig. C-3. Diagram of the drop test setup [21].

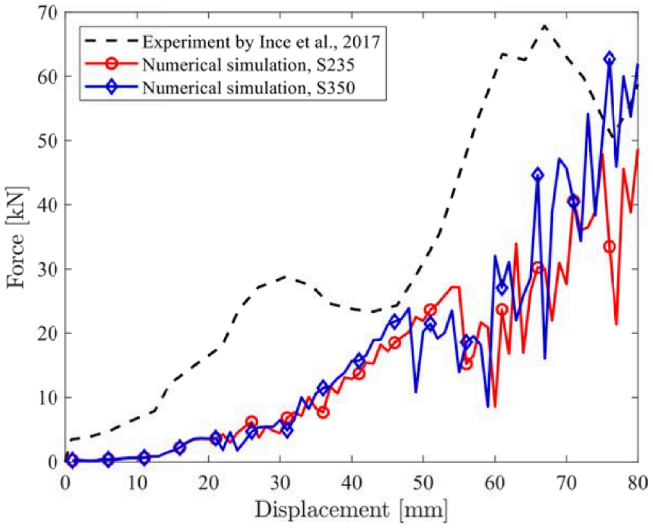

Fig. C-4. Total force versus displacement curves (Case 2).

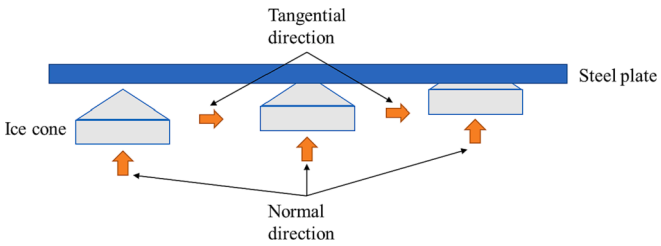

Fig. D-1. An ice cone sliding along a steel plate.

Appendix D:. Simulations of moving ice loads experiment

The VUMAT user subroutine is also used to simulate the moving ice loads experiments in Quinton [5]. Still, we use the same ice properties in the simulation. A thick steel plate (12.7 mm) acts as the crushing surface. An ice cone with a cone angle of 30 degrees moves in both normal and tangential directions towards the thick steel plate, as shown in Fig. D-1. The selected experiment is the test ML3, with a normal test speed of 3.5 mm/s and a horizontal test speed of 100 mm/s.

The contact force is recorded during the simulation and is compared with the experimental results shown in Fig. D-2. The simulation result curve is higher than the experimental result curve, but these two curves are within the same quantity range. The discrepancies between the numerical and experimental results might be still reasonable, considering the unknown ice properties used in the tests.

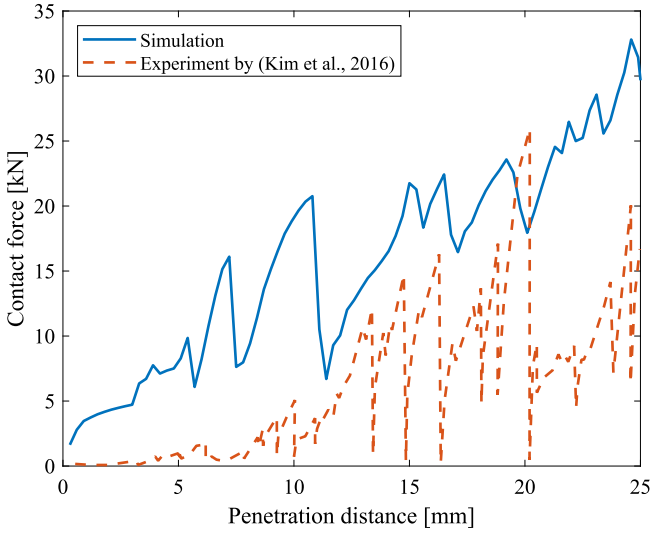

Fig. D-2. Contact forces in moving ice load condition.

References

[1] Hill B. Iceberg Right Ahead: Historic photographic evidence may lend support to a counterintuitive strategy for ship captains seeking to survive iceberg collisions. Cutting Edge 2016;2:9–10. http://cuttingedge.isgp.ubc.ca/journal/volume-2/2016/.
[2] Bassett V. Causes and Effects of the Rapid Sinking of the Titanic. Vicki Bassett College of Engineering University of Wisconsin; 2000.
[3] Foecke T. What really sank the Titanic? Mater Today 2008;11(10):48. https://doi.org/10.1016/S1369-7021(08)70224-4.
[4] Kim H, Quinton BWT. Evaluation of moving ice loads on an elastic plate. Mar struct 2016;50:127–42. https://doi.org/10.1016/j.marstruc.2016.07.007.
[5] Quinton BWT. Experimental and numerical investigation of moving loads on hull structures. Canada: Memorial University of Newfoundland; 2016. PhD dissertation.
[6] Quinton BWT, Daley C, Gagnon RE. Effect of Moving Ice Loads on the Plastic Capacity of a Ship's Structure. In: International Conference and Exhibition on Performance of Ships and Structures in Ice, 2010. Anchorage, Alaska.
[7] Liu Z, Amdahl J. On multi-planar impact mechanics in ship collisions. Mar Struct 2019;63:364–83. https://doi.org/10.1016/j.marstruc.2018.10.006.
[8] Liu Z, Amdahl J. A new formulation of the impact mechanics of ship collisions and its application to a ship–iceberg collision. Mar Struct 2010;23(3):360–84. https://doi.org/10.1016/j.marstruc.2010.05.003.
[9] Song M, Liu Z, Amdahl J. Estimation of ship bow-iceberg impact forces with consideration of the sliding effect. In: 28th International Ocean and Polar Engineering Conference. 2018.
[10] Dolny J. Methodology for defining technical safe speeds for light ice-strengthened government vessels operating in ice. Ship Structure Committee, editor. Houston; 2017.
[11] Daley C. Energy based ice collision forces. In: International Conference on Port and Ocean Engineering under Arctic Conditions, 1999. Helsinki, Finland.
[12] Ship AHS. Grounding: Analysis of Ductile Fracture, Bottom Damage and Hull Girder Response. Norway: Norwegian University of Science and Technology; 2008. PhD dissertation.
[13] Nguyen TH, Amdahl J, Leira BJ, Garrè L. Understanding ship-grounding events. Mar Struct 2011;24:551–69. https://doi.org/10.1016/j.marstruc.2011.07.001.
[14] Alsos HS, Amdahl J. Analysis of bottom damage caused by ship grounding. In 27th International Conference on Offshore Mechanics and Arctic Engineering, 2008. Estoril, Portugal.
[15] Quinton BWT. Lateral (sliding) motion of design ice loads on IACS polar classed structures. Ships Offshore Struct 2019;14(sup1):281–91. https://doi.org/10.1080/17445302.2019.1580844.
[16] IACS. Requirements concerning polar class, 2016. International Association of Classification Societies, London.
[17] Gagnon RE, Derradji-Aouat A. First Results of Numerical Simulations of Bergy Bit Collisions 598 with the CCGS Terry Fox Icebreaker. Proceedings of the 18th IAHR International Symposium on Ice. 2006.
[18] Ince ST, Kumar A, Paik JK. A new constitutive equation of ice materials. Ships Offshore Struct 2017;12(5):610–23.
[19] Ince ST, Kumar A, Paik DK, Paik JK. An advanced technology for structural crashworthiness of a ship colliding with an ice-ridge: numerical modelling and experiments. Int J Impact Eng 2017;110:112–22.
[20] Pedersen PT, Zhang S. On impact mechanics in ship collisions. Mar Struct 1998 Dec 1;11(10):429–49. https://doi.org/10.1016/S0951-8339(99)00002-7.
[21] Gagnon RE, Wang J. Numerical simulations of a tanker collision with a bergy bit incorporating hydrodynamics, a validated ice model and damage to the vessel. Cold Reg Sci Technol 2012;81:26–35. https://doi.org/10.1016/j.coldregions.2012.04.006.

[22] Yu Z, Amdahl J. A numerical solver for coupled dynamic simulation of glacial ice impacts considering hydrodynamic-ice-structure interaction. Ocean Eng 2021;226. https://doi.org/10.1016/j.oceaneng.2021.108827.
[23] Timco GW, Weeks WF. A review of the engineering properties of sea ice. Cold Reg Sci Technol 2010;60(2):107–29. https://doi.org/10.1016/j.coldregions.2009.10.003.
[24] Sanderson TJO. Ice mechanics and risks to offshore structures. 1988, United States.
[25] Gagnon RE. A numerical model of ice crushing using a foam analogue. Cold Reg Sci Technol 2011;65(3):335–50. https://doi.org/10.1016/j.coldregions.2010.11.004.
[26] Carney KS, Benson DJ, DuBois P, Lee R. A phenomenological high strain rate model with failure for ice. Int J Solids Struct 2006;43(25):7820–39. https://doi.org/10.1016/j.ijsolstr.2006.04.005.
[27] Liu Z, Amdahl J, Løset S. Plasticity based material modelling of ice and its application to ship–iceberg impacts. Cold Reg Sci Technol 2011;65(3):326–34. https://doi.org/10.1016/j.coldregions.2010.10.005.
[28] Coon MD, Knoke GS, Echert DC, Pritchard RS. The architecture of an anisotropic elastic-plastic sea ice mechanics constitutive law. J Geophys Res Oceans 1998;103(C10):21915–25. https://doi.org/10.1029/98JC01259.
[29] Pritchard RS. An Elastic-Plastic Constitutive Law for Sea Ice. J Appl Mech 1975;42(2):379–84. https://doi.org/10.1115/1.3423585.
[30] Shi C, Hu Z, Ringsberg J, Luo Y. Validation of a temperature-gradient-dependent elastic-plastic material model of ice with finite element simulations. Cold Reg Sci Technol 2017;133:15–25. https://doi.org/10.1016/j.coldregions.2016.10.005.
[31] Zhu L, Cai W, Chen M, Tian Y, Bi L. Experimental and numerical analyses of elastic-plastic responses of ship plates under ice floe impacts. Ocean Eng 2020;218:108174. https://doi.org/10.1016/j.oceaneng.2020.108174.
[32] Xu Y, Hu Z, Ringsberg JW, Chen G. Nonlinear viscoelastic-plastic material modelling for the behaviour of ice in ice-structure interactions. Ocean Eng 2019;173:284–97. https://doi.org/10.1016/j.oceaneng.2018.12.050.
[33] Sjölind SG. A constitutive model for ice as a damaging visco-elastic material. Cold Reg Sci Technol 1987;14(3):247–62. https://doi.org/10.1016/0165-232X(87)90017-6.
[34] Hunke EC, Dukowicz JK. An Elastic-Viscous-Plastic Model for Sea Ice Dynamics. J Phys Oceanogr 1997;27(9):1849–67.
[35] Ji S, Shen H, Wang Z, Shen HH, Yue Q. A viscoelastic-plastic constitutive model with Mohr-Coulomb yielding criterion for sea ice dynamics. Acta Oceanolog Sin 2005;24(4):54.
[36] Hibler W. A viscous sea ice law as a stochastic average of plasticity. J Geophys Res 1977;82(27):3932–8. https://doi.org/10.1029/JC082i027p03932.
[37] von Mises R. Mechanik der festen Körper im plastisch-deformablen Zustand. Nachrichten von der Gesellschaft der Wissenschaften zu Göttingen, Mathematisch-Physikalische Klasse 1913;4:582–92.
[38] Sain T, Narasimhan R. Constitutive modeling of ice in the high strain rate regime. Int J Solids Struct 2011;48(5):817–27. https://doi.org/10.1016/j.ijsolstr.2010.11.016.
[39] Tsai SW, Wu EM. A general theory of strength for anisotropic materials. J Compos Mater 1971;5:58–80.
[40] Riska K, Frederking R. Ice load penetration modelling. 1987.
[41] Kierkegaard H. Ship collisions with icebergs. Technical University of Denmark; 1993. PhD dissertation.
[42] Derradji-Aouat A. A unified failure envelope for isotropic fresh water ice and iceberg ice. In: Proceedings of ETCE/OMAE Joint Conference Energy for the New Millenium. 2000.
[43] Coulomb CA. Essai sur une application des regles de maximis et minimis quelques problemes de statique, relatits a larchitecture. Memoires de Mathematique de l'Academie Royale de Science 1776; 7: 343-387.
[44] Schulson EM, Nickolayev OY. Failure of columnar saline ice under biaxial compression: Failure envelopes and the brittle-to-ductile transition. J Geophys Res Solid Earth 1995;100(B11):22383–400. https://doi.org/10.1029/95JB02513.
[45] Schulson EM, Gratz ET. The brittle compressive failure of orthotropic ice under triaxial loading. Acta Mater 1999;47(3):745–55. https://doi.org/10.1016/S1359-6454(98)00410-8.
[46] Drucker DC, Prager W. Soil mechanics and plastic analysis for limit design. Q Appl Math 1952;10(2):157–65.
[47] Bhat SU, Choi SK, Wierzbicki T, Karr DG. Failure Analysis of Impacting Ice Floes. J Offshore Mech Arct Eng 1991;113(2):171–8. https://doi.org/10.1115/1.2919914.
[48] Pernas-Sánchez J, Pedroche DA, Varas D, López-Puente J, Zaera R. Numerical modeling of ice behavior under high velocity impacts. Int J Solids Struct 2012;49(14):1919–27. https://doi.org/10.1016/j.ijsolstr.2012.03.038.
[49] Bai Y, Wierzbicki T. Application of extended Mohr-Coulomb criterion to ductile fracture. Int J Fract 2010;161(1):1.
[50] Kõrgesaar M, Romanoff J. Influence of mesh size, stress triaxiality and damage induced softening on ductile fracture of large-scale shell structures. Mar struct 2014;38:1–17. https://doi.org/10.1016/j.marstruc.2014.05.001.
[51] Abaqus I. ABAQUS/Explicit User's Manual (version 2020). Dassault Systèmes Simulia Corp.: Providence, RI, USA; 2020.
[52] FSICR. Ice Class Regulations and the Application Thereof (Finnish-Swedish Ice Class regulations 2017), 2017; Finnish Transport Safety Agency.
[53] ISO/CD 19906. Petroleum and Natural Gas Industries — Arctic Offshore Structures, ISO TC 67/SC 7/WG 8. Final Draft International Standard, 2010. International Standardisation Organization, Geneva, Switzerland.
[54] Kim H, Daley C, Colbourne B. A numerical model for ice crushing on concave surfaces. Ocean Eng 2015;106:289–97. https://doi.org/10.1016/j.oceaneng.2015.07.020.
[55] DNV. Recommended Practice DNV-RP-C208, Determination of structural capacity by non-linear finite element analysis methods, 2019. Det Norske Veritas, Oslo, Norway.
[56] Liu Z. Numerical simulation of dropped container impacts with an offshore platform deck in the North Sea. Proc Inst Mech Eng, Part M: J Eng Maritime Environ 2021. https://doi.org/10.1177/1475090221993356.
[57] Kotisalo K, Kujala P. Ice load measurements onboard MT Uikku during the ARCDEV Voyage. Proceedings of POAC 1999:974–87.